Supplementary Materials for

Programmable metachronal motion of closely packed magnetic artificial cilia

Tongsheng Wang *et al.*

*Ye Wang. Email: y.wang2@tue.nl

This PDF file includes:

Supplementary Text
Figs. S1 to S14
Tables S1
Movies S1 to S7
References (1 to 2)

Other Supplementary Materials for this manuscript include the following:
Movies S1 to S7

Supplementary Text

SM 1: Femtosecond Laser Assisted Etching (FLAE) process

Design and generation of the laser toolpath

To design the laser toolpath, 3D models of the cilia and the channel structure are first made with CAD software, as shown in Fig. S1. Then the geometry is exported into Alphacam to create surfaces and lines on which the focal point of the laser needs to scan through. The toolpath also takes into account the size of the laser voxel. For the cilia mold, the entire volume of the machined part is scanned with overlapping voxels. For the microfluidic channel, hatch lines and planes are added to the geometry, effectively cutting the channel into smaller blocks to reduce the etching time.
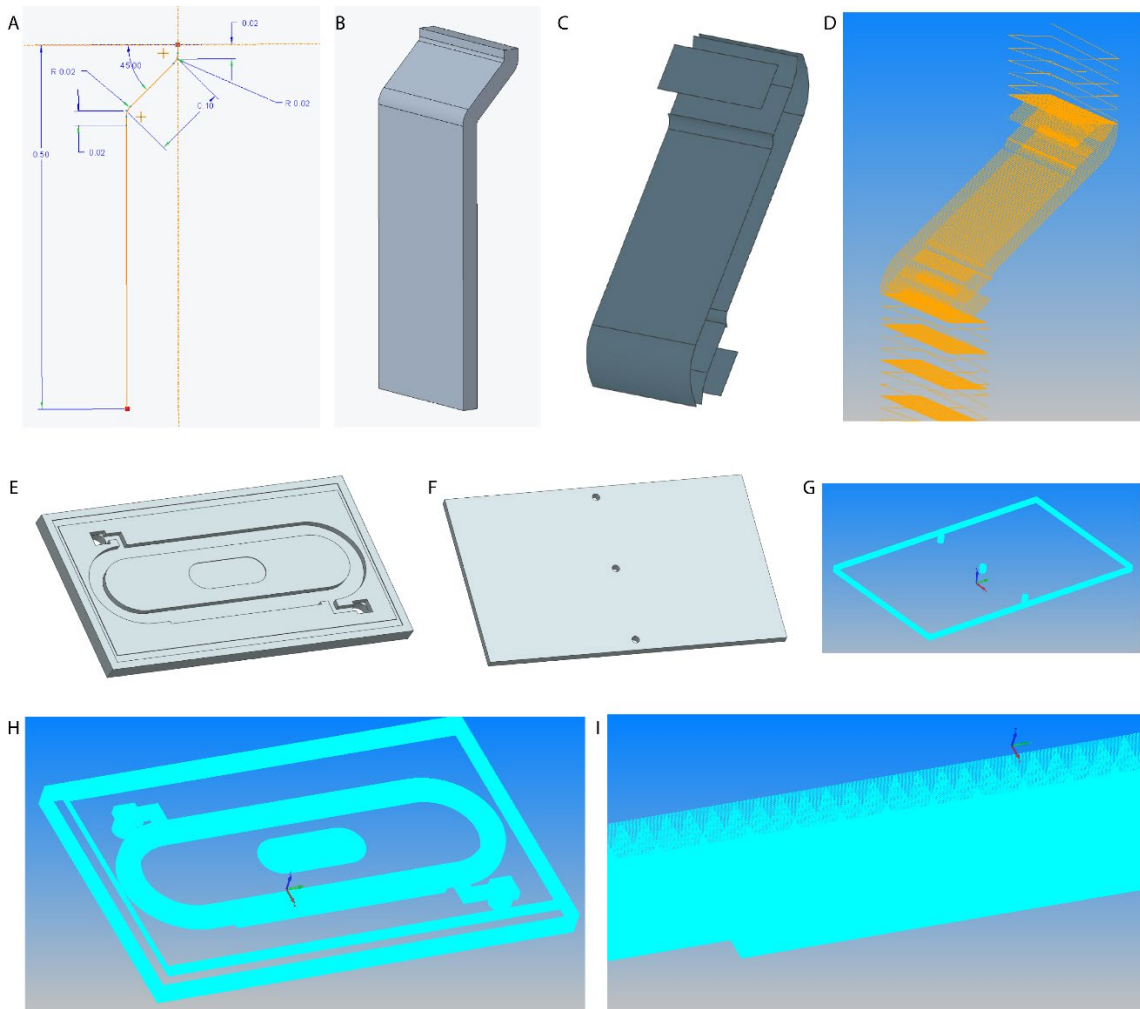

Fig. S1: **Geometry design and laser toolpath generation**. (A) The center line of the cilium looking from the side. (B) CAD model of the cilia body generated using the swept function in Siemens NX with a 24X200 μm rectangle through the center line. (C) The laser scanning surfaces generated based on the CAD model. (D) The generated laser tool path using Alphacam based on the scanning surfaces. (E) The design of the channel. (F) The design of the channel cap. (G) The laser tool path of the channel cap. (H) The laser tool path of the channel. (I) A closeup shot of the channel laser toolpath showing the hatch lines.

Fabrication procedure

A femtosecond laser machining system, as shown in Fig. S2 is used to fabricate the cilia molds and the microfluidic channels in fused silica. After laser machining, the slides are placed in potassium hydroxide solution (KOH) bath with ultrasonication to remove the machined parts. The accuracy of the laser machining process is about 1 µm.
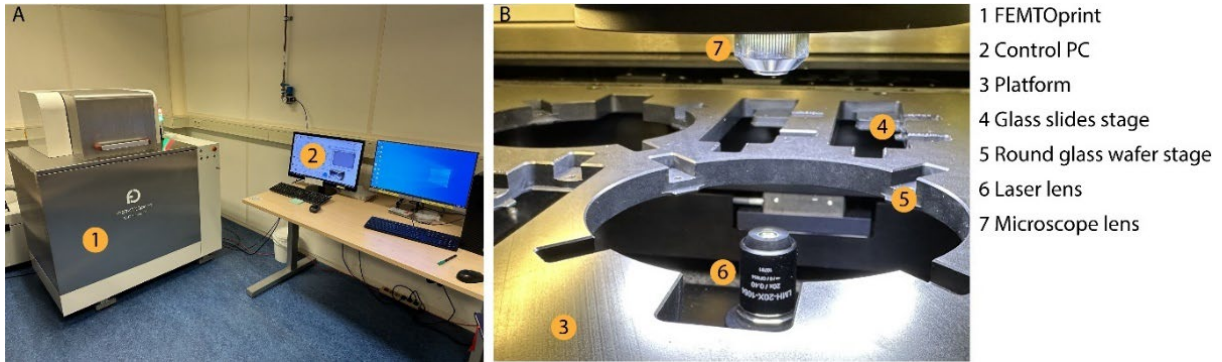

Fig. S2: **FEMTOprint f200 aHead machine**. (A) The machine and its control PC. (B) The workpiece holder platform. Glass slides and wafers can be mounted on the platform. The laser lens focus a beam of laser upwards. A microscope placed above the workpiece can be used to monitor the laser machining process.

For the etching process, the laser machined slide is first submerged a in a container filled with 45 wt% KOH, which is then placed in 85 °C ultrasound bath with the ultrasound intermittently turning on for one minute every ten minutes. The etching speed is 130 µm/h for laser-machined part and 1µm/h for unmachined part. Therefore, high aspect ratio structures will typically have a tapered edge with a 0.5° taper angle, unless the laser path is designed to compensate that. The total etching time is around 7 hours for cilia molds, 5 hours for the channels, and 3 hours for the channel caps.

SM 2: Cilia fabrication process

Mixing of magnetic particles and SIBS

The pure SIBS is mixed with magnetic powder using an extruder-mixer as shown in Fig. S3. The magnetic powder (carbonyl-iron powder, $\geq$ 99.5%, particle size 5-9 µm, Sigma-Aldrich) account for 70% of the weight of the final mixture. During mixing, the temperature is set to 150 °C, the counter rotating screws have the same rotation speed of 100 rpm, and the materials are mixed for 10 minutes before releasing.
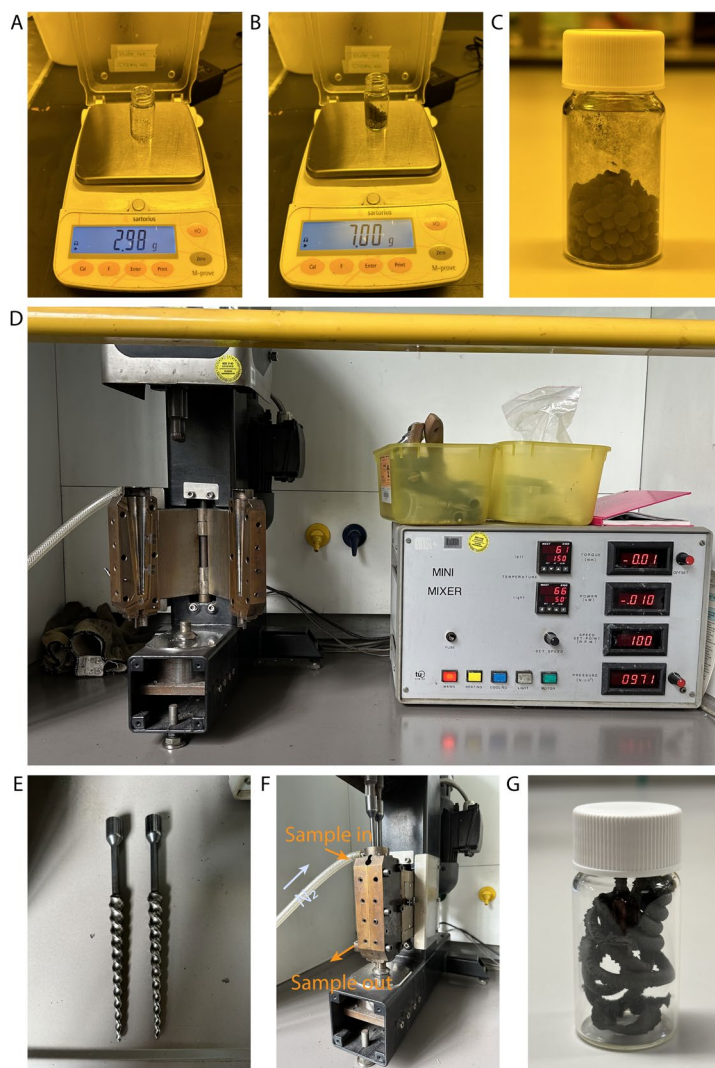
Fig. S3: **A typical process of creating magnetic SIBS.** (A) 3 gram pure SIBS. (B) 7 gram carbonyl-iron powder. (C) Pre-mixing of the SIBS and magnetic powder. (D) The twin-screw extruder-mixer. (E) The screws used for mixing. (F) Picture of the extruder-mixer during mixing. The sample is fed in from the upper inlet and discharged from the lower outlet after it is fully mixed. Nitrogen is continuously flowing into the mixing chamber at a low flow rate. (G) The mixed magnetic SIBS.

Transfer molding

Molding is performed using a hydraulic press fitted with hot plates (Specac, see Fig. S4). Custom made molds made of brass are used as inserts between the plates for making the thin film precursor layers (Fig. S5) for the cilia fabrication. These molds consist of a round flat plate with milled grooves of varying depths. In our study, we have two molds: one for producing pure SIBS films, with grooves having higher depths, and another for magnetic SIBS films, with grooves of lower depths.
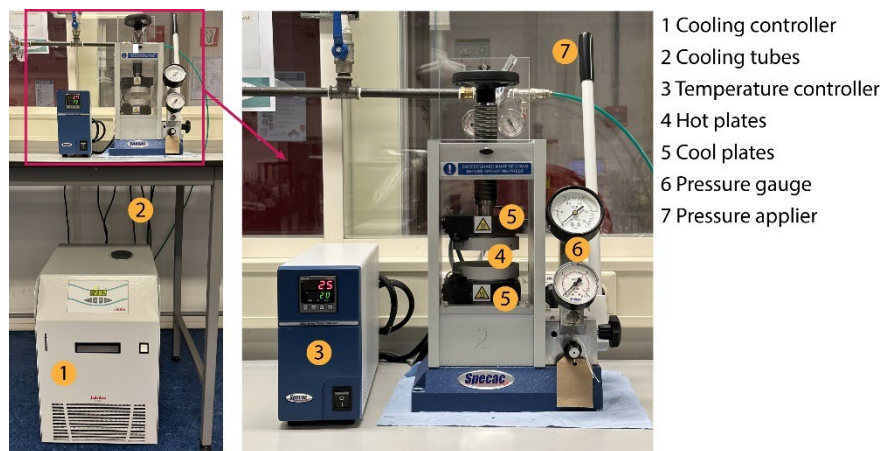
Fig. S4: **The hot press used for transfer molding**. The machine contains a cooling system, heating system, and a manual hydraulic press.
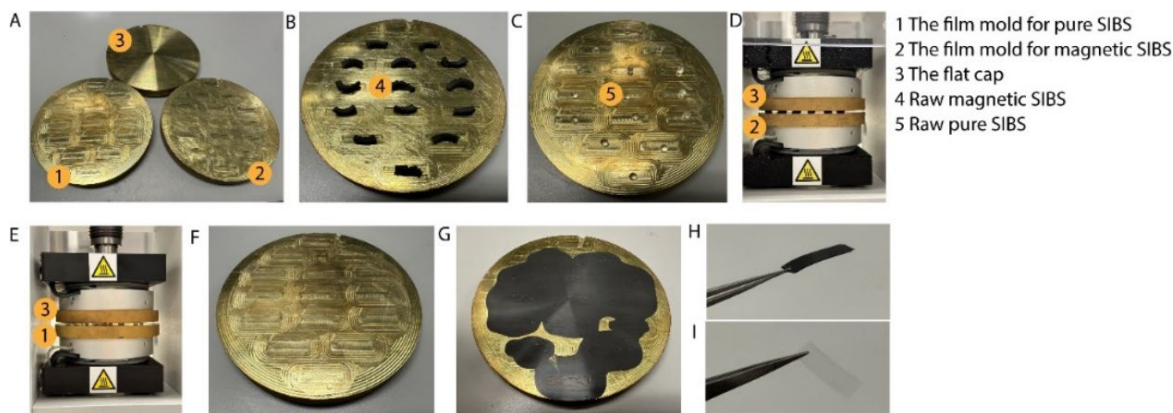

Fig. S5: **The precursor film fabrication process.** (A) The brass molds for making thin films. (B) The raw magnetic SIBS placed in the grooves. (C) The raw pure SIBS placed in the grooves. (D) The molding process of magnetic SIBS using the hot embossing. (E) The molding process of pure SIBS. (F)The molded pure SIBS. (G) The molded magnetic SIBS. (H) Magnetic SIBS film cut and demolded. (I) Pure SIBS film cut and demolded.

The steps involved in creating pure and magnetic SIBS films are identical. First, raw SIBS pellets were placed above the grooves of the brass mold. Next, a round flat brass plate was used to cover it, and the mold is placed into the press, which is then heated to 180 °C. After allowing the material to soften for approximately 3 minutes, a force of 40 kN was applied, and the temperature was then gradually lowered to 45 °C in approximately 45 minutes. Afterwards, the pressure is released and the resulting thin film can be peeled away from the molds and cut into desired shapes with a blade. After the films are made, they are molded again using the cilia mold made with FLAE and the same hot press. The process is shown in Fig. S6.
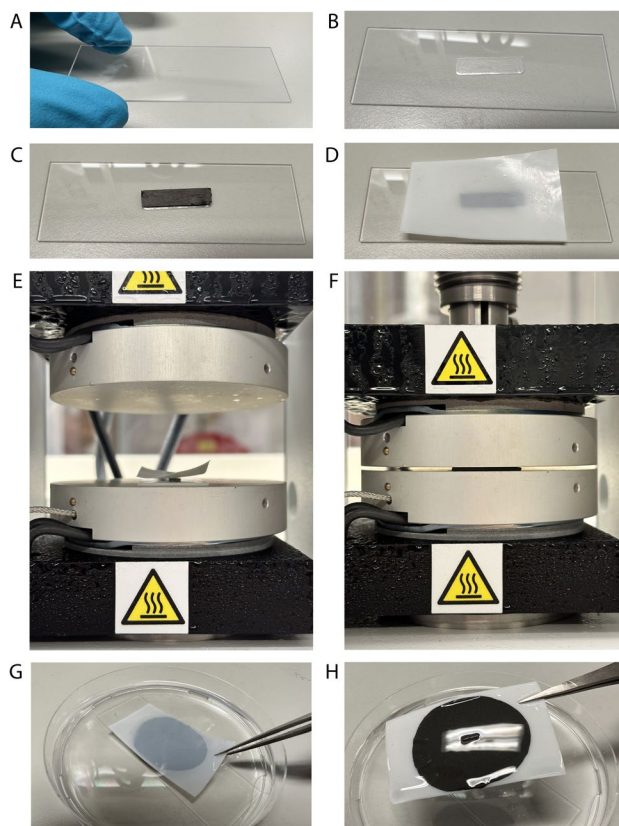
Fig. S6: **Cilia fabrication process.** (A) The cilia mold after etching and silanisation. (B) Placing the pure SIBS film on the mold. (C) Placing the magnetic SIBS film on the pure SIBS film. (D) Placing a 0.25 mm thick PTFE sheet on the mold. (E) Transferring the materials to the hot press and set the temperature to 130 °C. (F) Applying 4 kN force to the materials for 1 minutes and then lower the temperature to 90 °C. (G) Submerging the mold in isopropanol and demolding. (H) The demolded cilia.

Several parameters play a crucial role in determining the proportion of magnetic and non-magnetic components in the fabricated cilia. These parameters include the thickness of the precursor layers (both magnetic and non-magnetic), the applied heating temperature, and the magnitude of the pressing force. Among these, the thickness of the precursor layers is identified as the most significant factor influencing the outcome. Figure S7 illustrates the effects of varying these layer thicknesses. Regarding the heating temperature, an increase in temperature tends to soften the material, thereby enhancing its flowability. This enhancement is beneficial for the distribution of the material into the mold. However, excessively high temperatures may result in the viscosity being too low, preventing the magnetic layer from adequately filling the mold and leading to the production of entirely non-magnetic cilia. The pressing force is another influential factor. An increase in this force aids in the incorporation of the magnetic component into the cilia. Nonetheless, an overly high pressing force could result in an excessively thin substrate, complicating the demolding process due to the substrate's fragility. The parameters shown in this paper have been optimized from experience, however, further optimization or improvement of fabrication process might be needed for other geometries, or more precise control of the magnetic filling ratio.
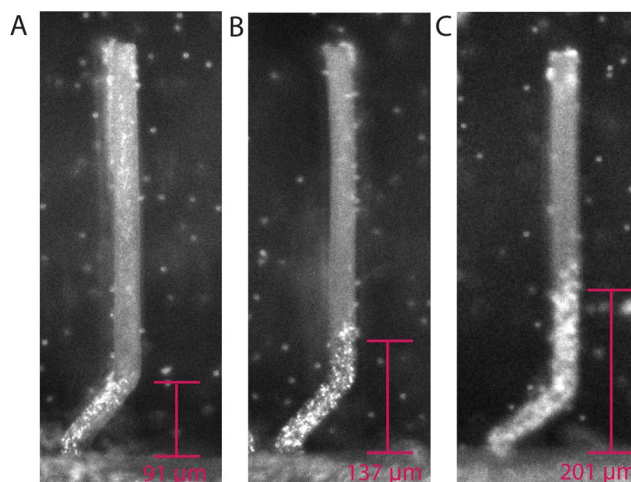
Fig. S7 **The results with different heights of precursor layers.** (A-C) The height of the precursor non-magnetic layer is fixed at 280 µm, while the height of the precursor magnetic layer varies as 60, 70, and 80 µm, respectively.

The versatility of the technique allows us to design cilia arrays with predetermined phase angles and wavelengths. Fig. S8 shows cilia arrays with angle differences of the root from 10° to 60° with the same designs of magnetic base and nonmagnetic body.

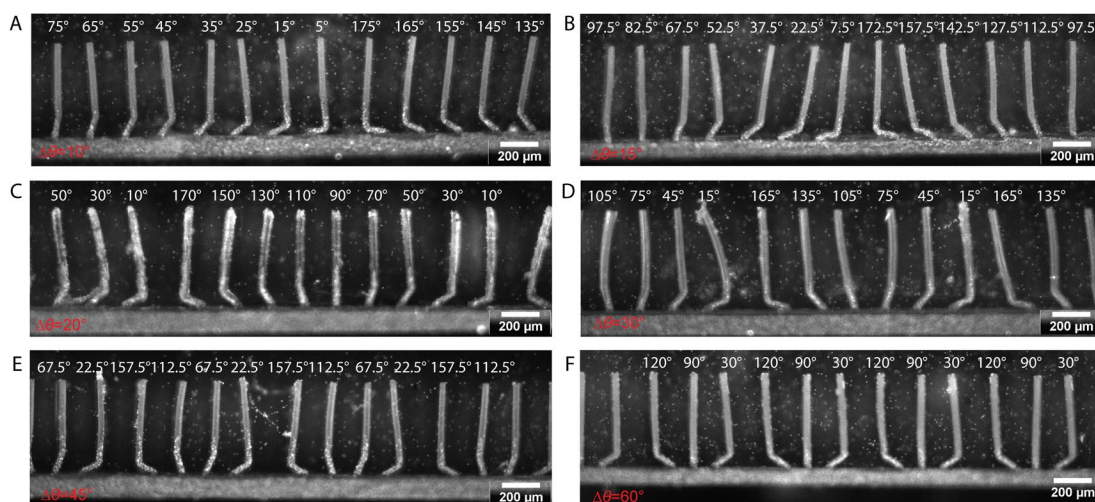Fig. S8 **Artificial cilia with various angle differences of the magnetic root.** (A-F) Angle difference of 10°, 15°, 20°, 30°, 45° and 60°, respectively.

SM 3: Cilia chip integration and fluid filling

Cilia integration

After the cilia patches were demolded, they were cut into 0.4 mm wide and 2 mm long stripes and placed sideways into the designated area of the channel, with its base facing the channel sidewall to which it must be attached. A small drop of low viscosity epoxy glue (Araldite 2020) was added to the gap between cilia patch and the glass surface, and the surface tension helped to spread the glue and flatten the cilia patch to align with the channel bottom (perpendicular to the

chip). The glue then was allowed to completely cure for 6 hours at room temperature or 2 hours at 65 °C until the hardening of the glue.

For sealing the channel, a cap with glue filling holes (made with FLAE) was bonded with the cilia-integrated channel. A small amount of the same epoxy glue mentioned above was placed on the filling holes and allowed to spread between the gaps. The surface tension ensures that only the gaps are filled with glue and not the channels.
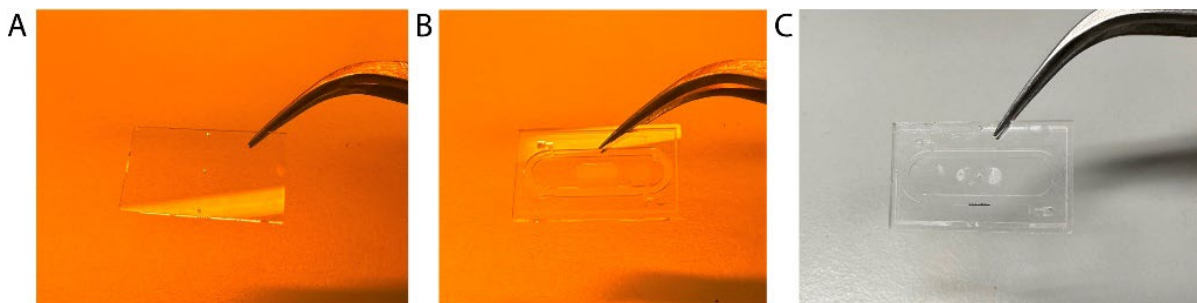

Fig. S9: **The cilia integration process.** (A) The channel cap. (B) The channel. (C) The integrated chip with the cilia patch seen at the lower part. First two images were taken inside a cleanroom.

Preparation of the tracer particle dispersion and filling of the chip

To achieve neutral buoyancy of the tracer particles (Polystyrene, 5 µm, carboxyl surface, 10 wt%, microParticles GmbH), 20 wt% glycerol solution in DI water was prepared as the carrier fluid. The resulting density is 1059 kg/m^3, and the dynamic viscosity is 1.98×10^{-3} Pa·s.

30 µl particle suspension was added to 30 ml carrier fluid, resulting in a concentration of 0.01 wt%. The density-matched mixture was then placed in an ultrasonic bath under degas mode for 10 minutes. The mixture is stable without sedimentation for at least 2 months at room temperature.

To fill the chip with the tracer particle suspension, it is first filled with isopropanol using a pipette, as the low surface energy of isopropanol enables it to spread into the gap between cilia without entrapment of air bubbles. DI water was then injected to replace isopropanol. And lastly, the particle solution was injected and the two openings were sealed with silicone adhesive tapes.

For cleaning and storing the chip after the experiment, the tapes were removed and the suspension was washed out first with isopropanol and then with DI water. The chip was then submerged in DI water for long term storage to prevent the cilia from collapsing and irreversibly bonding with each other.

SM 4: Magnetic actuator and recording parameters

Magnetic actuator

A magnetic actuator, as shown in Fig. S10, was built for actuating the cilia at high frequencies. To achieve sufficient and stable magnetic field at all frequencies, a permanent magnet Halbach array was used instead of an electromagnet. 16 neodymium magnets (10×10×40 mm) were used to generate a uniform field of 0.22 Tesla in the center. The array is driven by a DC motor with an encoder through a timing belt connection to allow light passing through the optical path. The

encoder is controlled by the laptop to monitor and control the speed of the motor. The chip is then placed in the middle plane of the array, where the cilia patch is situated at the center of the circle to ensure maximum homogeneity of the field.
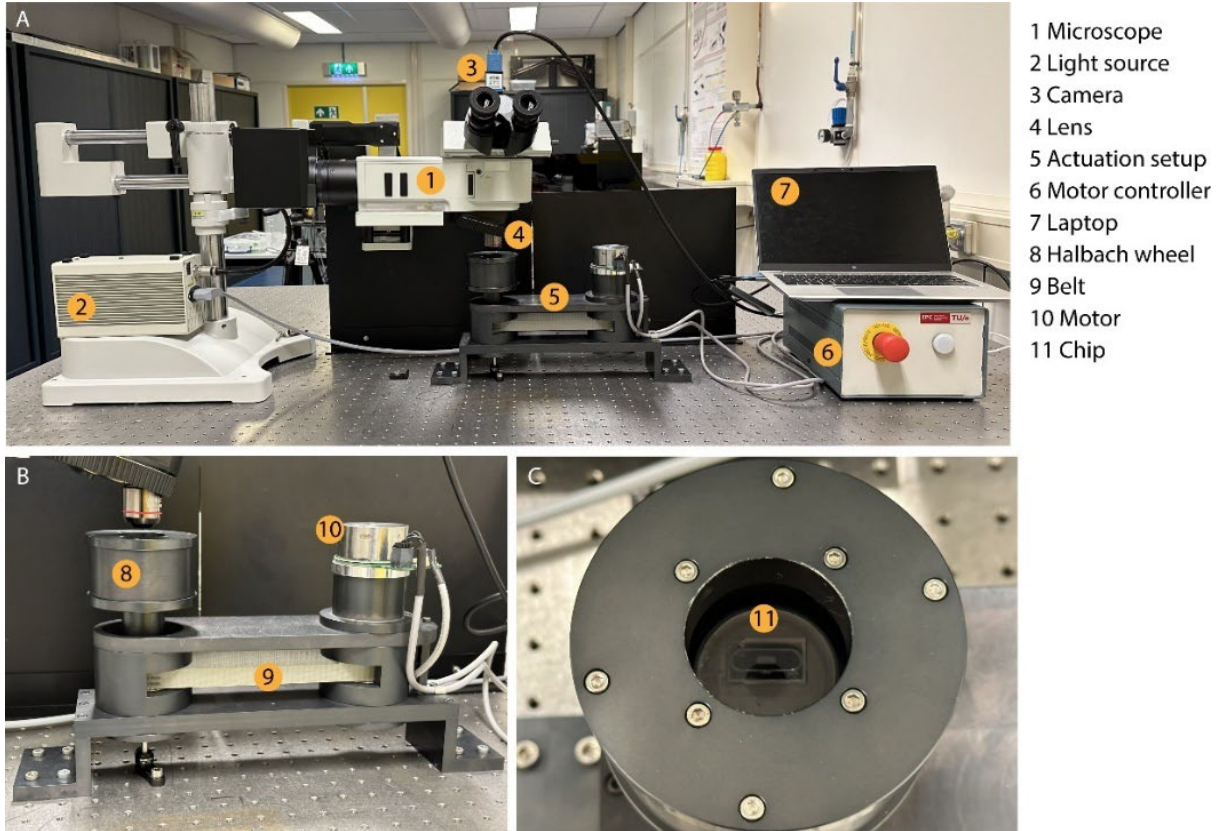

Fig. S10: **Experiment setup.** (A) The entire experiment setup consists of a microscope, the magnetic actuator, and a computer. (B) The magnetic actuator consists of a DC motor, a Halbach wheel and other mechanical components for the connection. (C) The chip placed on the chip stage holder in the central area of the Halbach wheel.

Recording setup

The raw data collected in this study is mainly videos captured by cameras. The detailed information of the data collection is shown in Table S1.

Table S1 **Experimental and recording parameters.**

Measurement objective	Lens	Camera	ROI	Rotation frequency (Hz)	Cilia beating / actuation frequency (Hz)	Video capture speed (fps)	Exposure time (sec)
Fully developed flow	Olympus LMPLFL N5XBD	IMAGINGSOURCE DMK 33UX252	1	1	2	1	1/1000
				10	20	10	
				20	40	20	
				30	60	30	
				40	80	40	
				50	100	50	
Instantaneous flow field			2	1	2	180	
				1	2	2	

Long-term particle trajectory				10	20	20	
				20	40	40	
				30	60	60	
				40	80	80	
				50	100	100	
Cilia motion	Olympus LMPLFL N20XBD	Phantom VEO 1310 high-speed camera		1	2	100	1/42000
				10	20	1000	
				20	40	2000	
				30	60	3000	
				40	80	4000	

SM 5: Net flow velocity prediction from COMSOL® simulation

In the 2D simulation, we have kept the channel height and the cilia geometry the same as in the experiments. Before calculating the net flow, the cilia dynamic and the local vortices were first compared with experimental results for validation, as shown in the main text with Fig. 2 and 3. Due to the laminar nature of the fully developed channel flow away from the cilia array, COMSOL® simulations were set up without simulating the whole channel length as in the experiments, but only a sufficiently long, open ended channel that the cilia driven flow is allowed to develop into a complete parabolic profile. In this way, we ensure the reliability of the results, while saving the computation cost.

To translate the simulated flow rate to the actual predicted flow rate in the channel, a simple conversion is performed. The channel length in the simulation is 10 mm, with the cilia array occupying the middle 2 mm, so the effective length of the channel is about 8 mm. In the experiment, the total length of the recirculating channel is 36 mm excluding the cilia patch, hence 4.5 times the simulated channel length. Due to the laminar nature of the flow, it is then reasonable to assume that the flow resistance is proportional to the channel length, therefore the estimated flow rate is calculated by dividing the simulated flow rate by 4.5. The resulting volume flow rate at actuation frequency of 2 Hz is about 0.066 µl/min, compared to 0.039 µl/min in the experiments. Considering the difference in 2D (single parabolic profile) and 3D (semi-double parabolic profile), we can say that the simulation result matches reasonably well with the experiments.

Using the COMSOL® model, we can predict the net flow rate generated by cilia arrays with various phase differences, as shown in Fig. S11. It can be seen that the largest flow rate appears around an angle difference of 45° and it is roughly twice as large compared with the rate for the 10° angle difference. The result shows that we can further increase the flow rate by optimizing the angle difference parameter for applications that require larger flow rates.
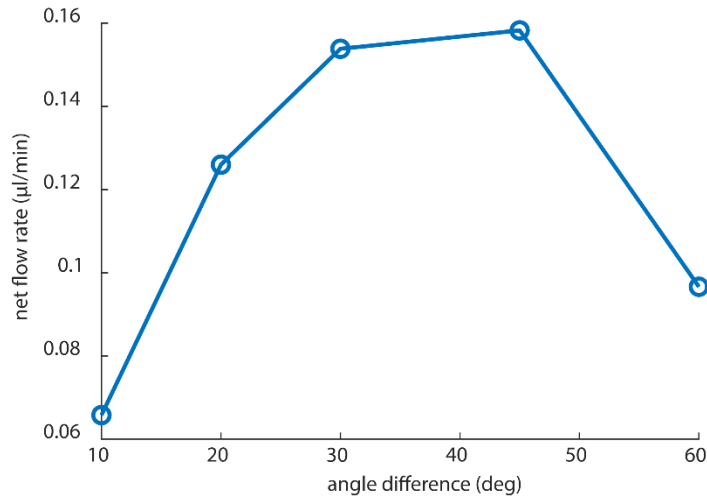
Fig. S11: **Results from COMSOL simulations showing the net flow rates generated by cilia arrays with different angle differences of the magnetic root**.

SM 6: Phase shift between neighboring cilia

Fig. S12 shows the derived phase shift values in degrees between each cilia pair in the divergent and convergent arrays, using the data shown in Fig. 2F and G in the main text.
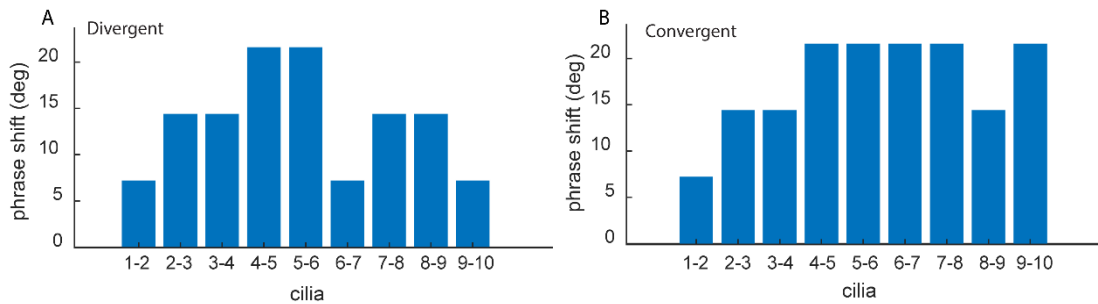

Fig. S12 **Characterization of the phase shift between neighboring cilia in the divergent and convergent arrays from Fig. 2F-G in the main text.**

SM 7: 1DOF model of the cilia motion

Model development

To better understand the relevant physical forces and to help design the angle differences in the cilia arrays, we have developed a simple 1DOF model. First, the structure of the model was derived from a combination of first principles modeling and heuristics with some unknown parameters, which were then determined using the data from COMSOL® simulation. Using this model, we can estimate the ratio between relevant forces and the movement of the cilia based on the magnetic actuation and the base angles.

Based on experimental observations of cilia beating behavior, it can be regarded as a nonlinear elastic beam oscillating under a periodic torque from the magnetic field, while the inertia of the

11

beam and the damping forces are also considered. Inspired by the work of Philip Holmes(1), we have employed a modified form of the Duffing's oscillator to model this behavior:

$$J\ddot{\phi}(t)+\delta'\dot{\phi}(t)+k'\phi(t)+\alpha'\phi^3(t)=T\big(t,\phi(t)\big) \tag{1}$$

with $\phi(t)$ representing the cilia's beating angle, $\dot{\phi}(t)$ and $\ddot{\phi}(t)$ representing the first and second order time derivatives. The positive direction is defined as clockwise, with zero angle in the direction of the y axis, as shown in Fig. S13.
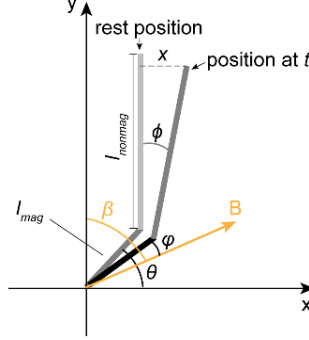

Fig. S13: **Diagram showing the parameters for the 1DOF model**

The terms on the lefthand side of the equation are torques generated by inertia, damping, linear and nonlinear elasticity, respectively. The elastic torque is modeled as a third order polynomial without the quadratic term, because the elastic torque should be axisymmetric about y, and such a form should be sufficient to capture the stress-strain response of the beam under relatively small bending angles. The parameters J, δ', k', α' are the fitting coefficients for these terms, which can be derived based on simulation results from COMSOL® or experimental data. On the righthand side, $T(\mathrm{t}, \phi(t))$ denotes the magnetic torque derived from first principles(2):

$$T(t)=\frac{Al}{2\mu_0}\big(\chi_{para}-\chi_{perp}\big)B^2(t)\sin 2\varphi(t) \tag{2}$$

were A is the cross sectional area of the cilia, l is the length of the magnetic part of the cilia, $\mu_0 \approx 4\pi \times 10^{-7}$ H/m is magnetic permeability of free space, χ_{para} and χ_{perp} are the magnetic susceptibility parallel and perpendicular to the cilia. $\varphi(t)$ is the relative angle between magnetic field and the magnetic root of the cilia, which is defined as:

$$\varphi(t)=\beta(t)-\phi(t)-\left(\frac{\pi}{2}-\theta\right) \tag{3}$$

with the angle of the magnetic field:

$$\beta(t)=\arctan\frac{B_x(t)}{B_y(t)} \tag{4}$$

where $B_x(t)$ and $B_y(t)$ are the x and y components of the magnetic field $B(t)$, and θ is the magnetic root angle of cilia. Combining equations (1) to (4), we have:

$$\ddot{\phi}(t) + \delta\dot{\phi}(t) + k\phi(t) + \alpha\phi^3(t) = \gamma B^2(t)\sin\left\{2\left[\arctan\frac{B_x(t)}{B_y(t)} - \phi(t) - \left(\frac{\pi}{2} - \theta\right)\right]\right\} \tag{5}$$

where the coefficients are normalized by J ($\delta = \delta'/J$, $k = k'/J$, $\alpha = \alpha'/J$, $\gamma = (Al / 2J\mu_0)$ (χ_{para} - χ_{perp})) and let $J = 1$ to make the model linear-in-the-parameters.

System identification

As described above, part of the model is heuristic, and therefore those model parameters need to be estimated from data. In the model, the time-dependent inputs are B_x and B_y and the output is ϕ. For the identification of the coefficients, we use ϕ calculated based on COMSOL® simulation for the cilium with the magnetic root angle θ of 45° ($\pi/4$ rad) as described below:

$$x + l_{mag}\cos\frac{\pi}{4} = l_{mag}\cos\left(\frac{\pi}{4} - \phi\right) + l_{nonmag}\sin\phi \tag{6}$$

where x is the x component of the cilia tip displacement, l_{nonmag} is the length of the nonmagnetic part, and l_{mag} is the length of the magnetic part. Since the largest angle $\phi \approx 14°$ (0.244 rad) and $l_{mag} / l_{nonmag} \leq 0.32$, the ϕ can be approximated by:

$$\phi = \arcsin\frac{x}{l_{nonmag}} \tag{7}$$

The magnetic field is given by:

$$B_x(t) = B_0\sin(2\pi ft), \text{ and } B_y(t) = B_0\cos(2\pi ft) \tag{8}$$

respectively, where B_0 is the magnitude of the magnetic flux density. Then we use System Identification Toolbox in MATLAB® to estimate the parameters. The *nlgreyest* function was used, which is an ODE-based parameter estimation algorithm using a data-driven prediction error minimization technique. To use this algorithm, the model needs to be represented in the form of a system of first-order differential equations. We convert our model to the following structure:

$$\dot{\phi}_2 = -\delta\phi_2 - k\phi_1 - \alpha\phi_1^3 + \gamma B^2\sin\left\{2\left[\arctan\frac{B_x}{B_y} - \phi_1 - \left(\frac{\pi}{2} - \theta\right)\right]\right\}, \quad \phi_1 = \phi, \quad \phi_2 = \dot{\phi}_1 \tag{9}$$

After identification, we got $\delta = 1\times10^6$ [1/s] $k = 3\times10^7$ [1/s^2], $\alpha = -2\times10^6$ [1/(rad^{2}s^2)], $\gamma = 2.1\times10^8$ [(A^{2}m^{2}rad)/(N^{2}s^2)].

The identified model was then used to estimate the contributions of different types of torques on the cilia dynamics. It can also be used to calculate the phases and amplitudes of the motion of cilia with root angle θ other than 45°. The results are plotted in Fig. 2F-G in the main text.

Torque analysis using the 1DOF model

The model is used to predict the time-dependent responses of cilia with different root angles and under different actuation frequencies. We first investigated the $\phi(t)$ of cilia with $\theta = 45°$ under different frequencies, as shown in Fig. S14A. The beating amplitude decreases quickly when the frequency increases. The result matches well with the experimental measurements shown in Fig. 2D-E, where ϕ has been converted to the horizontal displacement of the tips of the cilia using

13

Equation (7). Fig. S13B shows $\phi(t)$ of cilia with different root angles from 15° to 165°. It can be seen that they have a regular phase difference of 60° in their motion, while having a root angle differences between each neighboring cilia of 30°. This is caused by the fact that the cilia are superparamagnetic, which causes them to beat twice in one rotation cycle of the magnetic field.

By performing comparisons between the different terms in equation (5), The model can also shed light on relative importance of different factors. Use the cilia with base angle of 45° for an example, comparing magnetic torque defined as

$$T_{mag} = \gamma B^2(t) \sin\left\{ 2\left[\arctan\frac{B_x(t)}{B_y(t)} - \phi(t) - \left(\frac{\pi}{2} - \theta\right)\right]\right\} \qquad (10)$$

and elastic torque as

$$T_e = k\phi(t) + \alpha\phi^3(t) \qquad (11)$$

as shown in Fig. S14C. The sign of T_e is inverted in the figure because in the equation they have the same signs but their directions are opposite physically. It can be seen that the peak magnetic torque remains roughly the same, independent of actuation frequencies, while the peak elastic torque decreases because of the decrease of ϕ. The time response of the viscous torque defined as

$$T_{vis} = \delta\dot{\phi}(t) \qquad (12)$$

and the elastic torque T_e are plotted in Fig. S14D. The sign of T_{vis} is also inverted. It shows that the viscous torque quickly increases due to the rise of beating velocity under higher frequencies, which overtakes elastic torques at a rather moderate frequency (around just a few Hz) as the dominant factor, together with the magnetic torque, for the dynamics of cilia. This also shows why the fluid inertia is relatively small in our case, compared with full magnetic cilia in literature, as the fluid drag on the cilia is so dominant over the elasticity that the cilia cannot reach a high speed in the elastic stroke. Note that (with some simple calculation) the inertia torque term is very small compared with other terms, so for the dynamics of the cilia motion, inertia is not important (the same cannot be said for the fluid being driven by the cilia, which can be seen from the Reynold's number being close to 1, shown in Fig. 2 H and I in the main text). Similar conclusions hold true for cilia with other base angles as well.
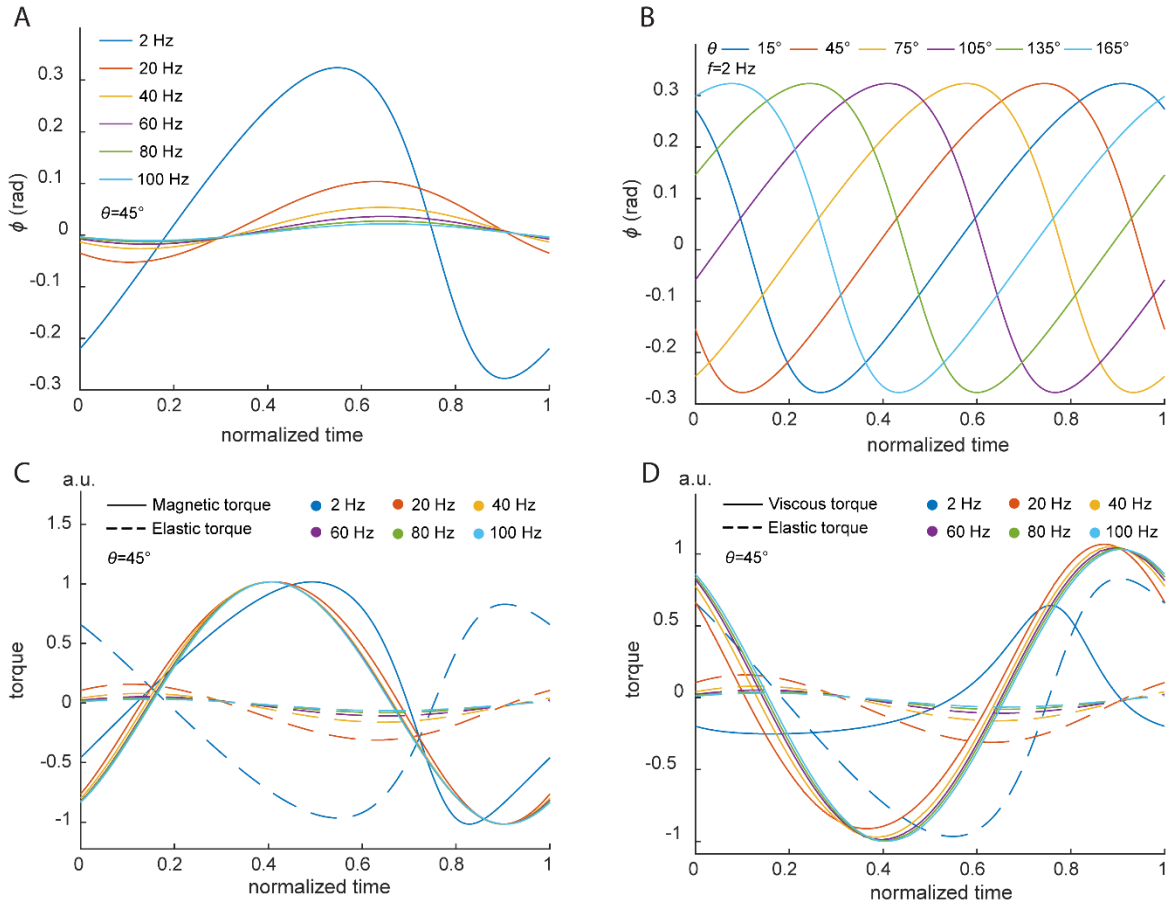
Fig. S14: **Results of the motion and torque analysis using the 1DOF model.** (A) the angle of cilia deflection ϕ with the root angle $\theta = 45°$ under different beating frequencies. (B) ϕ of cilia with different root angle θ under beating frequency of 2 Hz. (C) the magnetic torque and elastic torque of cilia with $\theta = 45°$ under different frequencies. (D) the viscous torque and elastic torque of cilia with $\theta = 45°$ under different frequencies. All values for the time on the horizontal axes have been normalized by the oscillation period time to better visualize the changes in phase and amplitude of various quantities. All figures show one beating cycle during steady state; at normalized time 0, the magnetic field points in the y direction. Note that the cycle finishes when the clockwise rotating magnetic field is in the -y direction (half a field rotation cycle corresponds to one cilia beating cycle).

Reference

1.   J. Guckenheimer, P. Holmes, *Nonlinear oscillations, dynamical systems, and bifurcations of vector fields*. (Springer Science & Business Media, 2013), vol. 42.
2.   F. Fahrni, Magnetic polymer actuators for microfluidics. PhD thesis, Eindhoven University of Technology (2009).

Movie S1.

Higher time-resolution imaging showing time-dependent flow structures with divergent and convergent arrays actuated at 2 Hz. The particles perform cyclic motion with net displacement over time. Walking vortices can be observed during each beating cycle of the cilia.

Movie S2.

Stroboscopic imaging showing particle trajectories over longer durations with the convergent array. The video capture rate is the same as the actuation rate of cilia, so the differences in consecutive frames show the net displacement of particles. Stable vortices can be observed from these trajectories.

Movie S3.

Same as Movie 2, but with the divergent array.

Movie S4.

Simulation results showing the time-dependent streamlines and velocity map.

Movie S5.

Particle tracking at ROI1 location on the chip with the divergent cilia array actuated at 2 Hz.

Movie S6.

Simulation results of different cilia spacing.

Movie S7.

Simulation results of different angle differences of the magnetic root.